







Article

Tuning the Co Oxidation State in $\text{Ba}_{0.5}\text{Sr}_{0.5}\text{Co}_{0.8}\text{Fe}_{0.2}\text{O}_{3-\delta}$ by Flame Spray Synthesis Towards High Oxygen Evolution Reaction Activity

Dino Aegerter ^{1,*}, Mario Borlaf ², Emiliana Fabbri ^{1,*}, Adam H. Clark ¹,
Maarten Nachtegaal ¹, Thomas Graule ² and Thomas J. Schmidt ^{1,3}

¹ Energy and Environment Research Division, Paul Scherrer Institute PSI, Forschungsstrasse 111, CH-5232 Villigen PSI, Switzerland; adam.clark@psi.ch (A.H.C.); maarten.nachtegaal@psi.ch (M.N.); thomasjustus.schmidt@psi.ch (T.J.S.)

² Laboratory for High Performance Ceramics, Empa-Swiss Federal Laboratories for Materials Science and Technology, CH-8600 Dübendorf, Switzerland; marioborlaf@gmail.com (M.B.); thomas.graule@empa.ch (T.G.)

³ Laboratory of Physical Chemistry, ETH Zurich-Swiss Federal Institute of Technology in Zurich, CH-8093 Zürich, Switzerland

* Correspondence: dino.aegerter@psi.ch (D.A.); emiliana.fabbri@psi.ch (E.F.);
Tel.: +41-56-310-5321 (D.A.); +41-56-310-2795 (E.F.)

Received: 31 July 2020; Accepted: 19 August 2020; Published: 1 September 2020



Abstract: The perovskite-type oxide $\text{Ba}_{0.5}\text{Sr}_{0.5}\text{Co}_{0.8}\text{Fe}_{0.2}\text{O}_{3-\delta}$ (BSCF) is known as a highly active and stable oxygen evolution reaction (OER) electrocatalyst composited out of non-noble metals. The possibility of using the scalable flame spray synthesis (FSS) technique for the production of BSCF nanoparticles intensified the interest in this material for a future application in an alkaline water electrolyzer. A possible scale-up would require the optimization of the synthesis parameters to maximize the production rate. To further understand the influence of the synthesis parameters of the tunable FSS on the OER activity of BSCF, a systematic study was carried out by producing BSCF with different total metal concentrations (C_{TM}), flow rates of the precursor solution (FR_{PS}) and of the dispersion gas (FR_{DG}). This study reveals that all three parameters have a direct impact on the OER activity of BSCF—measured in a rotating disc electrode (RDE) setup—due to the controllability of the initial Co and Fe oxidation state—indicated by X-ray absorption spectroscopy (XAS) measurements—and with that also of the oxygen vacancy concentration in the as-synthesized BSCF. This controllability enables the optimization of the OER activity of BSCF and emphasizes the importance of having Co in a lower initial oxidation state for reaching a high electrocatalytic performance.

Keywords: alkaline water electrolyzer; water splitting; oxygen evolution reaction; perovskite-type oxide; flame spray synthesis; rotating disc electrode; X-ray absorption spectroscopy; Co K-edge; oxygen vacancy; oxy(hydroxide)

1. Introduction

One of the biggest challenges of this century—the replacement of the 89% share of the world primary energy consumption based on non-renewable energy sources [1]—requests for efficient energy storage technologies to equilibrate the supply and demand of renewables. Despite the tremendous research effort in recent decades, no golden path solution has been presented to date, indicating that a combination of technologies specialized for different time- and size scales are required for solving this challenge. A possible part of a worldwide solution for the long-term and large-scale

storage of renewable produced surplus electricity is the so-called “Hydrogen Economy” [2]. In such an economy, hydrogen (H_2) acts as an energy vector [3] which is synthesized with renewable produced surplus electricity mainly via water electrolysis [4,5]. Therefore, the development of highly efficient electrolyzers is needed to be cost-competitive. The oxygen evolution reaction (OER)—the reaction at the anode of an electrolyzer—is one of the main reasons for the limited efficiency of this energy conversion device [6]. Improvements in electrocatalysts are required to minimize the overpotential of the OER and hence increase the overall efficiency, resulting in the low-cost production of H_2 . The ideal electrocatalysts combine not only high activity and stability, but should also be produced with inexpensive precursors and a scalable synthesis technique [7]. One promising candidate that can fulfil these demanding requirements is flame spray synthesized $Ba_{0.5}Sr_{0.5}Co_{0.8}Fe_{0.2}O_{3-\delta}$ (BSCF)—a member of the perovskite-type oxide family (ABO_3) [8–10]. BSCF shows not only a promising activity [8–14] and stability [8–10] in a rotating disc electrode (RDE) setup but also in an alkaline exchange membrane water electrolysis cell [8,9]. Moreover, the performance of BSCF does not originate from expensive noble metals such as iridium, ruthenium or platinum and can be produced with the scalable flame spray synthesis (FSS) technique—a well-known method for industrial manufacturing [15,16] of, e.g., carbon black [17] or Co-based nanomaterials [18,19].

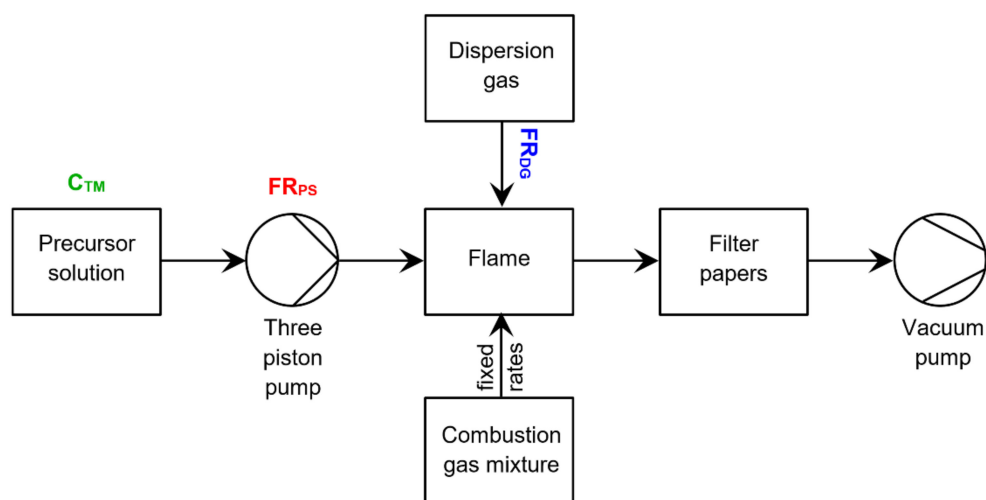
Generally, perovskite-type oxides such as BSCF are produced with the so-called sol-gel [14,20–24] or co-precipitation method [14,25,26]. Both synthesis routes have a significant disadvantage as both the sol-gel [9] and co-precipitation method [26] produce particles in the μm range. FSS is able to overcome this limitation by producing BSCF as nanoparticles with a scalable method [27]. However, the successful synthesis of low-cost BSCF required significant changes in the standard approach for FSS of perovskite-type oxide nanoparticles [27]. This standard approach includes the dissolution of metal-organic precursors in an organic solvent and then the combustion in a methane flame [28]. A disadvantage of this approach is how expensive metal-organic precursors are compared to nitrates, the most cost-effective metal precursors [29]. This aspect hinders the low-cost FSS of BSCF, especially because the precursors are in general the main cost driver (>50%) in a large-scale FSS nanoparticle production ($100 \text{ t}\cdot\text{year}^{-1}$) [30]. The use of nitrates as an inexpensive alternative is limited in this standard approach due to its relative low volatility as well as solubility in organic solvents [27]. Therefore, aqueous solutions are needed to increase the solubility of nitrates, which is necessary for a high production rate—an important parameter for a scale-up. These aqueous-based precursor solutions contain a larger share of non-combustible solvents such as water, effecting a decrease in the flame temperature due to the cooling effects during vaporization of these non-combustible components. This decrease in the flame temperature hinders the successful synthesis of the desired metal oxides [27]. Thus, a higher flame temperature is needed, which can be delivered with acetylene, since this fuel has a much higher energy density than a methane or propane flame [27]. In summary, the standard approach was changed from metal-organic to nitrate precursors, from organic to aqueous solvents and from a methane to an acetylene flame for a successful FSS of low-cost BSCF nanoparticles with a high specific surface area [27]. All these changes request a renewed systematic study on the optimization of the synthesis parameters to further understand their influence in this new FSS approach on BSCF with the perspective of using this material as an OER electrocatalyst in an alkaline water electrolyzer.

BSCF is produced for this purpose under different conditions by varying the three investigated synthesis parameters—the total metal concentration (C_{TM}), the flow rate of the precursor solution (FR_{PS}) and of the dispersion gas (FR_{DG}). This study reveals that all three parameters have a significant influence on the OER activity of BSCF, as shown in RDE measurements. X-ray absorption spectroscopy (XAS) measurements elucidate that the main reason for this strong influence lies in the controllability of the initial Co and Fe oxidation state in the as-synthesized BSCF batches through these synthesis parameters. An overlapping trend between the OER activity and the initial Co oxidation state is observed by reaching higher OER activity with a lower Co oxidation state produced with a lower C_{TM} , a higher FR_{PS} and a lower FR_{DG} . Therefore, the most OER active BSCF has Co, and to a smaller extent

Fe, in a lower initial oxidation state. This then accommodates a higher oxygen vacancy concentration in the BSCF.

2. Results

The effect of three flame spray synthesis (FSS) parameters was investigated on the properties of $\text{Ba}_{0.5}\text{Sr}_{0.5}\text{Co}_{0.8}\text{Fe}_{0.2}\text{O}_{3-\delta}$ (BSCF) as oxygen evolution reaction (OER) electrocatalyst. The three synthesis parameters of interest were the total metal concentration (C_{TM}) in the precursor solution, the flow rate of the precursor solution (FR_{PS}) and the flow rate of the dispersion gas (FR_{DG}). An overview of the FSS setup and the assigned parameters is shown in Scheme 1. A more detailed description of the setup is published in reference [27].



Scheme 1. Process flow diagram of the used flame spray synthesis (FSS) setup to indicate the three investigated synthesis parameters—total metal concentration (C_{TM}) in the precursor solution, flow rate of the precursor solution (FR_{PS}) and flow rate of the dispersion gas (FR_{DG}).

The total metal concentration (C_{TM}) is given as the sum of the concentration of all metal ions (Ba, Sr, Co and Fe) in the precursor solution. The flow rate of the precursor solution (FR_{PS}) determines how fast the precursor solution is injected into the flame and the flow rate of the dispersion gas (FR_{DG}) determines how fast the dispersion gas (O_2) is injected into flame. The dispersion gas is used in an FSS setup to form precursor solution droplets while entering the flame.

To investigate the effects of these three synthesis parameters on the synthesized BSCFs, one of these parameters was varied for different syntheses while holding the two other parameters constant in each of these syntheses. Finally, three different BSCF batches were produced for each synthesis parameter with one in common, resulting in seven different BSCF batches in total. The used values for each synthesis are summarized in Table 1.

The physical and structural features of all synthesized BSCF batches were analyzed with transmission electron microscopy (TEM). A representative TEM image of the common BSCF batch ($C_{\text{TM}} = 0.1 \text{ M}$, $\text{FR}_{\text{PS}} = 50 \text{ mL}\cdot\text{min}^{-1}$ and $\text{FR}_{\text{DG}} = 25 \text{ L}\cdot\text{min}^{-1}$)—the batch which is in common for all three synthesis parameter investigations—is shown in Figure 1 as exemplary for all BSCF batches. TEM images reveal roughly a particle size distribution between 5 and 15 nm. However, beside the small nanoparticles were bigger particles ($\sim 50 \text{ nm}$) visible in other TEM images for all synthesized BSCF batches as depicted in Figure S1 in the Supplementary Materials.

Furthermore, all BSCF batches were characterized with powder X-ray diffraction (XRD) and the specific surface area (SSA) was determined by applying the Brunauer–Emmett–Teller theory (BET) on N_2 adsorption isotherms. The electrochemical analysis included the measurement of the OER activity and the oxidation state of Co and Fe in the as-synthesized BSCF batches were identified with X-ray

absorption spectroscopy (XAS). In the following, the results are presented separately for each synthesis parameter in order of appearance during the synthesis.

Table 1. Summary of the condition variations for the $\text{Ba}_{0.5}\text{Sr}_{0.5}\text{Co}_{0.8}\text{Fe}_{0.2}\text{O}_{3-\delta}$ (BSCF) production to investigate the three flame spray synthesis parameters—total metal concentration (C_{TM}) in the precursor solution measured in $\text{mol}\cdot\text{L}^{-1}$ or M, flow rate of the precursor solution (FR_{PS}) measured in $\text{mL}\cdot\text{min}^{-1}$ and flow rate of the dispersion gas (FR_{DG}) measured in $\text{L}\cdot\text{min}^{-1}$. The results of the effect of each parameter on BSCF are presented in Sections 2.1–2.3.

Synthesis Parameters	2.1. C_{TM}	2.2. FR_{PS}	2.3. FR_{DG}
C_{TM}/M	0.1 ¹ , 0.2 or 0.3	0.1	0.1
$\text{FR}_{\text{PS}}/\text{mL}\cdot\text{min}^{-1}$	50	50 ¹ , 30 or 10	50
$\text{FR}_{\text{DG}}/\text{L}\cdot\text{min}^{-1}$	25	25	25 ¹ , 35 or 45

¹ Same BSCF batch, and thus three BSCF batches for each parameter with one in common (seven in total).

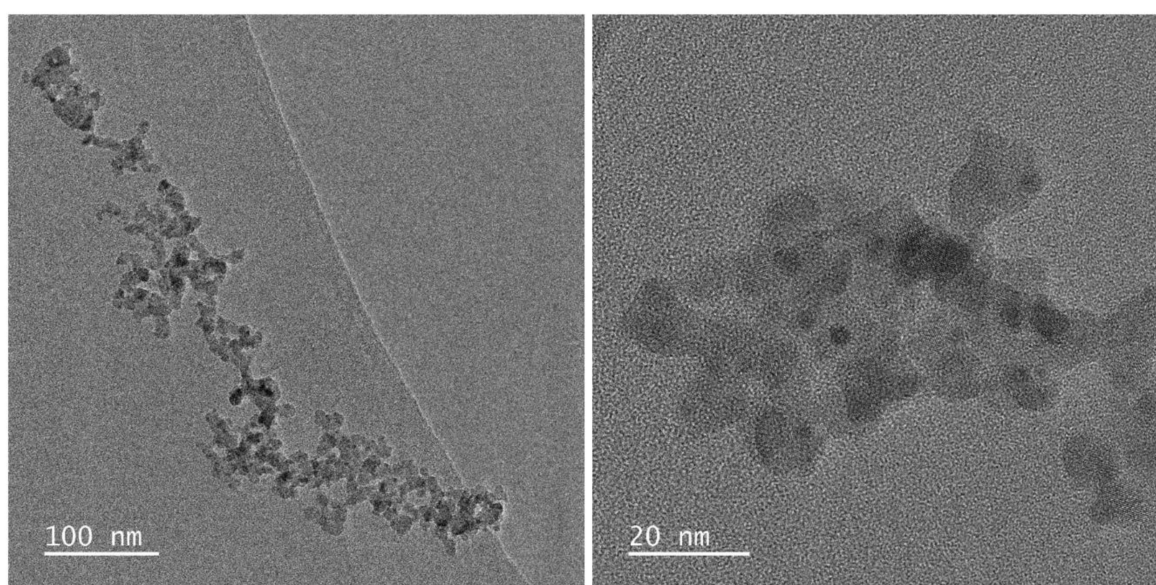


Figure 1. Representative transmission electron microscopy (TEM) images of the common BSCF batch ($C_{\text{TM}} = 0.1 \text{ M}$, $\text{FR}_{\text{PS}} = 50 \text{ mL}\cdot\text{min}^{-1}$ and $\text{FR}_{\text{DG}} = 25 \text{ L}\cdot\text{min}^{-1}$)—the batch which is in common for all three synthesis parameter investigations—as an example for all BSCF batches. The particle size ranges roughly between 5 and 15 nm.

2.1. Total Metal Concentration C_{TM}

Figure 2 shows the XRD patterns, the SSA_{BET} , the Tafel plot and the Co K-edge X-ray absorption near edge spectroscopy (XANES) spectra of the three BSCF batches produced with different C_{TM} of 0.1, 0.2 and 0.3 M while keeping the stoichiometry of the metals in $\text{Ba}_{0.5}\text{Sr}_{0.5}\text{Co}_{0.8}\text{Fe}_{0.2}\text{O}_{3-\delta}$ for all three syntheses constant ($\text{FR}_{\text{PS}} = 50 \text{ mL}\cdot\text{min}^{-1}$ and $\text{FR}_{\text{DG}} = 25 \text{ L}\cdot\text{min}^{-1}$).

The XRD patterns (Figure 2a) of the three BSCF batches look very similar and reveal a marginal influence of the C_{TM} as synthesis parameter on the crystallinity of BSCF. Overall, the XRD patterns show the characteristic peaks—primary and secondary phases—for flame-spray-synthesized BSCF [8–10]. The peaks associated with BSCF—the primary phase—overlap well with the reference (∇ ICSD: 185122). For a more detailed analysis of the FSS typical secondary phases, refer to Section S2 in the Supplementary Materials. The SSA_{BET} of the BSCF batches (Figure 2b) are all within the error of the measurements ($\Delta\text{SSA}_{\text{BET}} < 1 \text{ m}^2\cdot\text{g}^{-1}$) and hence show no significant dependence on C_{TM} . The Tafel plot (Figure 2c) reveals significantly higher OER activity (higher mass normalized current J at the same potential ($E_{\text{IR-free}}$) or lower $E_{\text{IR-free}}$ at the same J) with decreasing C_{TM} . The Tafel slope is marginally higher for 0.2 and 0.3 M compared to 0.1 M, possibly indicating a slightly different OER mechanism.

The Co K-edge XANES spectra (Figure 2d) indicates a clear trend towards lower oxidation state (shift in the Co K-edge towards lower energy at the same normalized intensity) in the as-synthesized BSCF batches with decreasing C_{TM} . The Co oxidation state in all three cases is between +2 and +2.67, as deciphered from comparing the relative energy position of the sample spectra to the standards (CoO and Co_3O_4). The insignificant difference in the position of the well aligned Co K-edge XANES spectra of the Co reference foil (Figure S3)—measured simultaneously with the samples—show that the observed shifts (Figure 2d) are indeed related to the change in C_{TM} as a synthesis parameter. The same trend is visible for the Fe K-edge (Figure S4a), but to a much smaller extent. The existence and measurability of the small Fe K-edge trend can be verified by comparing it with the simultaneously measured and aligned reference foil spectra (Figure S4d). The aligned reference foil spectra do not show any energy shift at the same normalized intensity, which confirms that the small Fe K-edge trend in the sample spectra does not originate from any misalignment. The Fe oxidation state in BSCF is, for all three cases, around +3, as based on its relative position compared to the standards (FeO and Fe_2O_3).

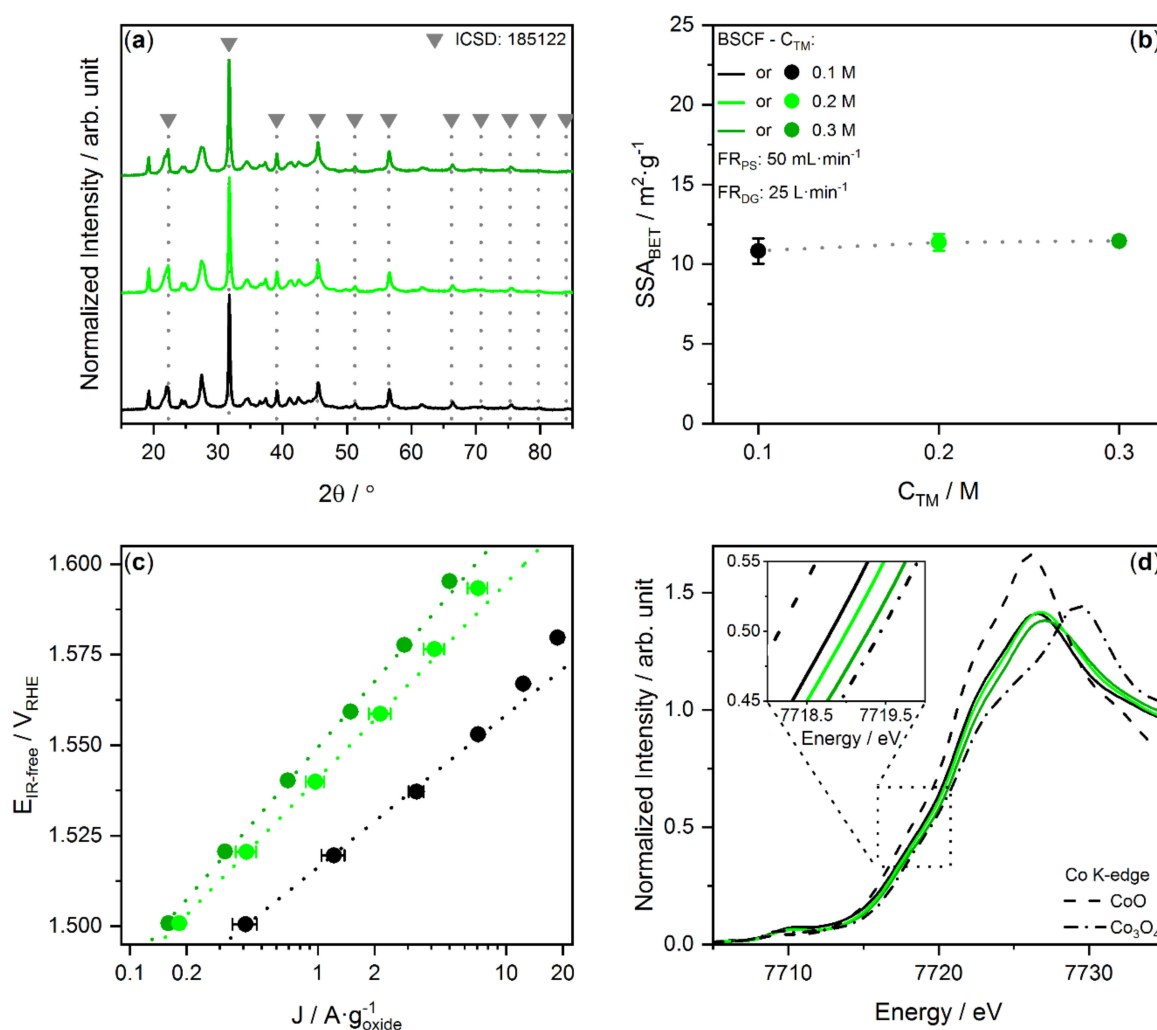


Figure 2. Summary of the influence of the total metal concentration (C_{TM}) in the range of 0.1 (— or ●), 0.2 (— or ●) and 0.3 M (— or ●) on flame spray synthesized $Ba_{0.5}Sr_{0.5}Co_{0.8}Fe_{0.2}O_{3-\delta}$ (BSCF): (a) Powder X-ray diffraction (XRD) patterns (▼ ICSD reference of BSCF: 185122); (b) Specific surface areas calculated with the Brunauer-Emmett-Teller equation (SSA_{BET}); (c) Tafel plot of the oxygen evolution reaction (OER) activities with linear fit (dotted line); (d) Co K-edge X-ray absorption near edge spectroscopy (XANES) spectra of the as-synthesized BSCF batches (standards: CoO (---) and Co_3O_4 (-·-)). For all cases: Flow rate of the precursor solution (FR_{PS}) = $50 \text{ mL} \cdot \text{min}^{-1}$ and dispersion gas (FR_{DG}) = $25 \text{ L} \cdot \text{min}^{-1}$.

2.2. Flow Rate of the Precursor Solution FR_{PS}

The summary of the analysis for the three BSCF batches produced with different FR_{PS} of 50, 30 and 10 $\text{mL}\cdot\text{min}^{-1}$ ($FR_{DG} = 25 \text{ L}\cdot\text{min}^{-1}$ and $C_{TM} = 0.1 \text{ M}$) is shown in Figure 3.

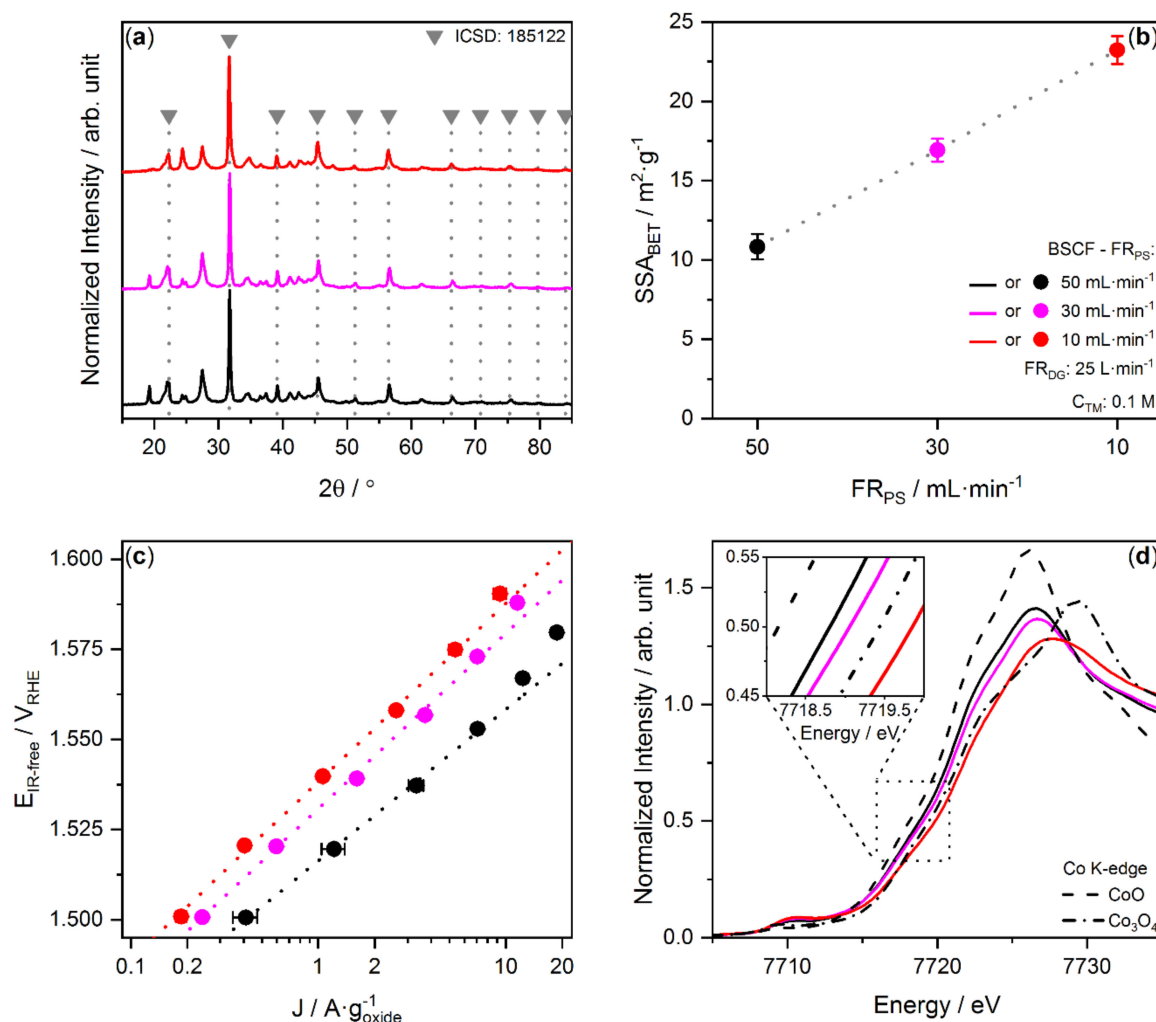


Figure 3. Summary of the influence of the flow rate of the precursor solution (FR_{PS}) in the range of 50 (— or ●), 30 (— or ●) and 10 $\text{mL}\cdot\text{min}^{-1}$ (— or ●) on flame spray synthesized BSCF: (a) Powder XRD patterns (∇ ICSD reference of BSCF: 185122); (b) SSA_{BET} ; (c) Tafel plot of the OER activities with linear fit (dotted line); (d) Co K-edge XANES spectra of the as-synthesized BSCF batches (standards: CoO (—) and Co_3O_4 (—•—)). For all cases: $FR_{DG} = 25 \text{ L}\cdot\text{min}^{-1}$ and $C_{TM} = 0.1 \text{ M}$.

FR_{PS} as synthesis parameter has a negligible influence on the crystalline phase of BSCF (Figure 3a). However, the secondary phases are partially enhanced with increasing FR_{PS} , especially the ones which are associated most likely to Ba- and Sr-based carbonates and nitrates at low 2θ angles (Figure S2). A higher FR_{PS} leads to a significant decrease in the SSA_{BET} (Figure 3b) which is well known for flame-spray-synthesized BSCF [27] or non-BSCF materials [16,28,31,32]. The FR_{PS} has a strong influence on the OER activity, resulting in a BSCF with a higher electrocatalytic activity when produced with a higher FR_{PS} (Figure 3c). In different words, the higher the powder production rate, the higher the OER activity of BSCF—an outstanding result for a possible scale-up. Slightly lower Tafel slopes are observed when the FR_{PS} is increased. The initial Co oxidation state—accessible with the XANES spectra at the Co K-edge (Figure 3d)—is lower in BSCF produced with a higher FR_{PS} . The relative position of the XANES of the samples compared to the standards show that the BSCF produced with the lowest FR_{PS} (10 $\text{mL}\cdot\text{min}^{-1}$) has a oxidation state clearly above +2.67, while the two

others are between +2 and +2.67, indicating an unequivocal difference in Co oxidation state among these samples (compare shifts in Figure 3d and Figure S3). The Fe K-edge shows the same trend but has a smaller shift (Figure S4b) and the oxidation state is around +3 as the Fe_2O_3 standard.

2.3. Flow Rate of the Dispersion Gas FR_{DG}

Figure 4 presents the summary of the analysis of BSCF produced with different FR_{DG} of 25, 35 and 45 $\text{L}\cdot\text{min}^{-1}$ ($\text{FR}_{\text{PS}} = 50 \text{ mL}\cdot\text{min}^{-1}$ and $C_{\text{TM}} = 0.1 \text{ M}$).

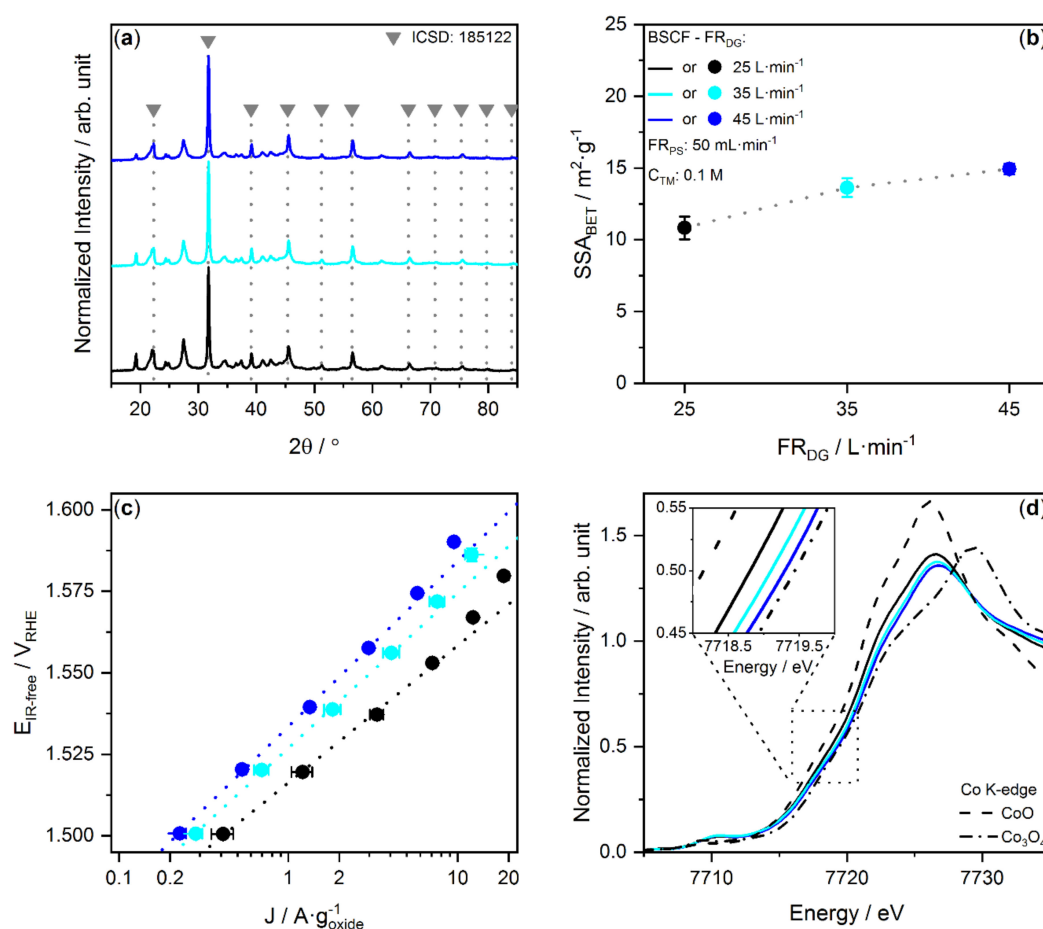


Figure 4. Summary of the influence of the flow rate of the dispersion gas (FR_{DG}) in the range of 25 (— or ●), 35 (— or ●) and 45 $\text{L}\cdot\text{min}^{-1}$ (— or ●) on flame spray synthesized BSCF: (a) Powder XRD patterns (▼ ICS reference of BSCF: 185122); (b) SSA_{BET} ; (c) Tafel plot of the OER activities with linear fit (dotted line); (d) Co K-edge XANES spectra of the as-synthesized BSCF batches (standards: CoO (—) and Co_3O_4 (—•—)). For all cases: $\text{FR}_{\text{PS}} = 50 \text{ mL}\cdot\text{min}^{-1}$ and $C_{\text{TM}} = 0.1 \text{ M}$.

The crystalline BSCF phase is, in all three cases, similar (Figure 4a). Several secondary phases are slightly enhanced when BSCF is produced with a lower FR_{DG} . These enhanced secondary phases are located in the XRD patterns at low 2θ angles and are most likely associated to Ba- and Sr-based carbonates and nitrates (Figure S2). A lower FR_{DG} produces in general materials with a lower SSA_{BET} [16,31–34], and BSCF is not an exception here (Figure 4b). This parameter has a strong influence on the OER activity of BSCF (Figure 4c). Higher mass normalized currents J at the same potential $E_{\text{IR-free}}$ and slightly smaller Tafel slopes are measured for BSCF that was produced with a lower FR_{DG} . The XANES at the Co K-edge indicate that the initial Co oxidation state is, in all three cases, between +2 and +2.67 while having a trend towards lower Co oxidation state when BSCF is produced with a lower FR_{DG} (Figure 4d). The Fe K-edge indicates an oxidation state around +3 in all three cases (Figure S4c) but showing a visible trend of a decreasing Fe oxidation state with decreasing FR_{DG} .

3. Discussion

TEM images in Figure 1 show the successful FSS of nanoparticles with a size distribution between 5 and 15 nm as known for BSCF [8–10]. These particles are most likely formed in the flame by evaporation (vaporization), nucleation and coagulation in the so-called gas-to-particle conversion [29,35]. However, larger particles (~50 nm) are also viewed as depicted in Figure S1. The origin of these larger particles is related to the nitrate precursors used for the synthesis and they are possibly formed through precipitation in the so-called droplet-to-particle conversion [29,35].

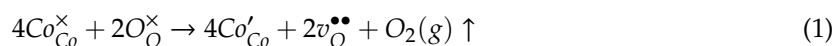
The three synthesis parameters do not have a significant influence on the crystallinity of BSCF but they have an impact on the secondary phases, especially the two flow rate parameters— FR_{PS} and FR_{DG} (Figures 2a, 3a and 4a). A higher FR_{PS} and a lower FR_{DG} increases the secondary phases, particularly the Ba- and Sr-based carbonates and nitrates. These findings can be explained considering the mechanism of the nanoparticle (primary phase) and secondary phase formation. The FSS mechanism can be separated in the following five steps: (1) precursor solution vaporization and combustion, (2) metal vapor formation, (3) metal oxide nanoparticles formation, (4) sintering and coalescence processes and (5) aggregation [28,35–37]. Secondary phase formation is possible due to parasitic side reactions along all reaction steps. A possible pathway for the formation of carbonates and nitrates starts with the precipitation of the metal nitrate precursors, particularly for barium nitrate, which has a relatively low solubility [27]. These precipitates decompose then in the flame to oxides [38] which can easily take up CO_2 and form carbonates at elevated temperatures at the cooling phase of the flame or in the exhaust gas [27]. The above-described five-step FSS mechanism for the nanoparticle formation occurs when the precursor solution is constituted by (mainly) organic solvents. However, in this study the precursor solution for all syntheses is mainly water-based and just 25 vol% is organic (refer to Section 4.1. Material Synthesis). This has a significant influence on the (1) precursor solution vaporization and combustion step of the nanoparticle formation mechanism. Vaporization will be more dominant than combustion for a mainly water-based precursor solution which enhances the probability of metal ion precipitation in the droplet as hydroxide, carbonate or nitrate. These precipitates will then decompose (or not), while forming the desired nanoparticle (or a secondary phase). The direct influence of FR_{PS} and FR_{DG} —to a smaller extent, also C_{TM} —on the secondary phase formation indicates that these synthesis parameters play a role in the above-mentioned processes. Indeed, the trends—favoring precipitation during the dominant vaporization phenomenon and thus the secondary phase formation—are obtained with a higher C_{TM} , a higher FR_{PS} and a lower FR_{DG} . The first parameter increases the probability of metal ion precipitation and the last two increase the droplet size of the precursor solution in the flame, meaning that not all will fully decompose, which then leads to secondary phase formation.

The observed SS_{BET} trends can be explained with the help of the FSS theory. It is well known and documented that a higher FR_{PS} and lower FR_{DG} produce nanoparticles with a smaller SS_{BET} , while the C_{TM} has only a marginal influence on the SS_{BET} for the used concentration range and production rates [16,27,28,31–34]. An important parameter that can describe this behavior is the high-temperature particle residence time (HTPRT) which determines the morphology and properties of flame-spray-synthesized materials [16]. A longer HTPRT extends the (4) particle sintering and coalescence step in the FSS, resulting in the production of larger particles [16,31]. The HTPRT is directly controlled by the FR_{PS} and FR_{DG} while the C_{TM} has a minor influence. A higher FR_{PS} increases the size of the flame and thus increases the HTPRT [16,31] while, in contrast, a higher FR_{DG} dilutes the flame and thus decreases the HTPRT [16,31–34]. This consideration can fully describe the SS_{BET} trends observed for all BSCF batches (Figures 2b, 3b and 4b). An additional effect is the formation of secondary phases which can pronounce the SS_{BET} trends even more. The XRD patterns (Figures 2a, 3a and 4a) indicate that BSCF batches with a lower SS_{BET} have also more secondary phases. This could be explained by the fact that secondary phases can theoretically form larger particles, as seen in Figure S1, leading to a smaller SS_{BET} , a value which is always an average over all produced particles.

In summary, the changes in the XRD patterns and the SS_{BET} trends as a function of the three parameters are fully understandable and can also be expected based on FSS theory. Not expected were

the OER activity trends observed for these three synthesis parameters (Figures 2c, 3c and 4c) based on the findings in XRD and SSA_{BET} . BSCF has a higher OER activity when produced with a lower C_{TM} , a higher FR_{PS} or a lower FR_{DG} . First, the variation in the C_{TM} did not affect the XRD patterns and SSA_{BET} of BSCF but has a significant influence on the OER activity. Second, the exact opposite OER activity trend was expected for the BSCF series produced with different FR_{PS} and FR_{DG} based on the influence seen in the secondary phase formation (XRD) and in the surface area (SSA_{BET}). In theory, BSCF with the lowest number of secondary phases and highest SSA_{BET} —produced with a low FR_{PS} or high FR_{DG} —should have the highest OER activity. In fact, Ba- and Sr-based carbonate and nitrate secondary phases are not OER active and they will most likely be washed away once in contact with the electrolyte [10]. Furthermore, OER is a surface specific reaction, meaning that a higher activity is expected for an electrocatalyst with a higher surface area. However, the highest OER active BSCF was produced with a high FR_{PS} and a low FR_{DG} and thus with a higher number of secondary phases and with a lower SSA_{BET} . Therefore, a piece is still missing for the explanation of the OER activity trends.

This missing piece can be found when considering the Co K-edge XANES spectra (Figures 2d, 3d and 4d). There is a clear match between the trends for the initial Co oxidation state and the OER activity (Figures 2c, 3c and 4c)—BSCF with Co cations in a lower oxidation state has a higher OER activity. The same holds true, to a smaller extent, for Fe (Figure S4a–c), since the trend in the initial Fe oxidation state is the same but the shifts in the Fe-K edge are smaller compared to those measured for the Co K-edge. This match in these trends has already been observed for BSCF [8–13] or non-BSCF perovskite-type oxides [8–10,13,39], but this is the first time that it is shown that the initial Co oxidation state in BSCF—and, with that, its OER activity—can be directly tuned by changing synthesis parameters. The reason for this connection between Co oxidation state in BSCF and its OER activity lies in the concentration of oxygen vacancies [8]. BSCF [40–46] or perovskite-type oxides in general [47–50] have a great ability to accommodate oxygen vacancies. The occurrence of oxygen vacancies in a perovskite-type oxide requires at least one of the two charge compensation possibilities on the A- and B-site cations. Charge neutralization within this oxide is achieved either by the formation of A- and/or B-site deficiencies or by the partial reduction in the A- and/or B-site cations. The observed decrease in the Co oxidation state of BSCF produced with a lower C_{TM} , a higher FR_{PS} and a lower FR_{DG} has to be charge-compensated with an increase in the oxidation state of another metal—most likely Fe—and/or with the formation of oxygen vacancies. Based on that fact, that the BSCF with a more reduced Co (Figures 2d, 3d and 4d) also incorporates Fe with a slightly lower oxidation state (Figure S4a–c) indicates that Fe does not act here as charge compensator. Therefore, the oxygen vacancy concentration remains a plausible option for the charge compensation of the strongly reduced Co. This concept can be exemplary visualized in a reaction equation written in the Kröger-Vink notation as



where four Co^{+3} atoms are reduced to Co^{+2} while releasing one O_2 molecule and forming two oxygen vacancies [45]. In summary, the more OER active BSCF (Figures 2c, 3c and 4c) has Co, and partially Fe, in a lower initial oxidation state while accommodating more oxygen vacancies. The BSCF with a higher number of oxygen vacancies—produced with a lower C_{TM} , a higher FR_{PS} and a lower FR_{DG} —can then interact with the electrolyte and form, over a lattice OER (LOER)/OER process [6], to a greater extent, a self-assembled and superficial oxy(hydroxide) layer, the real active site of BSCF, as discussed in detail in reference [8].

The remaining question is why do these synthesis parameters have a direct influence on the Co, and partially Fe, oxidation state, and thus on the oxygen vacancy concentration? First of all, the properties of BSCF depend on two important parameters—the temperature and the oxygen partial pressure during the synthesis [41,42,45,46]. The Co oxidation state decreases, and thus the oxygen vacancy concentration increases in BSCF at higher temperatures and at lower oxygen partial pressures [41,42,45,46]. Both aspects play an important role during the FSS. The temperature and reaction time—the time when the particles are exposed to the high temperature in the flame—depends

again on HTPRT. The particles remain for a longer time in the high-temperature regions of the flame with a longer HTPRT—reached with a higher FR_{PS} [16,31] and a lower FR_{DG} [16,31–34]—leading to the production of a more oxygen-deficient BSCF with Co, and partially Fe, in a lower oxidation state. It is notable that the increase in the FR_{PS} increases not only the size of the flame but also the speed of the materials within the flame. A higher HTPRT is mainly reached with a higher FR_{PS} because the volume of the flame is over-proportionally increased compared to the speed of the materials, as nicely depicted in reference [31]. The C_{TM} can also have a direct impact on the flame temperature. A lower C_{TM} always increases the heat input per metal ion, which can lead then to the production of BSCF with a lower Co oxidation state and with a higher oxygen vacancy concentration. The oxygen partial pressure in the flame is most likely directly dependent on the FR_{DG} , since pure oxygen was used as a dispersion gas (refer to Section 4.1 Material Synthesis). Therefore, a lower FR_{DG} would then lead to a lower partial pressure in the flame, thus producing also an oxygen-deficient BSCF with Co, and partially Fe, in a lower oxidation state.

At this point, it is important to mention that the dependence of the Co oxidation state, and thus the oxygen vacancy concentration, in BSCF, from the parameters' temperature and oxygen partial pressure, was revealed in the literature in so-called in situ experiments [41,42,45,46]. In comparison to that, all experiments in this study were performed ex situ, meaning that the BSCF batches were not characterized while being in the flame but after they were cooled down to room temperature and under atmospheric pressure. Nevertheless, different properties regarding the Co and Fe oxidation state, and thus of the oxygen vacancy concentration in BSCF, were elucidated in these ex situ measurements. Therefore, the different flame conditions—set with the three synthesis parameters—lead to changes in the properties of the synthesized BSCF which are partially irreversible and thus measureable in the performed ex situ measurements at room temperature and under atmospheric pressure. This partial irreversibility of the Co oxidation state and thus the oxygen vacancy concentration in BSCF was already observed in reference [46], where a different oxidation state was measured at 300 K before and after a heating step to 1073 K. This means that the lower Co oxidation state reached at higher temperature (1073 K) was partially maintained even though the sample was cooled down back to room temperature. In conclusion, it is justified to use in situ results from literature—at high-temperature and low-oxygen partial pressures—to explain, in this study, the properties of BSCF measured ex situ—at room temperature and under atmospheric pressure. Moreover, the temperature in an acetylene/oxygen mixture as used in the flame spray synthesis for all BSCF batches (refer to Section 4.1. Material Synthesis) can reach up to 3000 °C, while most of the studies in the literature about Co oxidation state and oxygen vacancies are performed up to around 1200 °C [41,42,45,46]. Furthermore, the cooling-down process in a flame spray synthesis is very fast ($\gg 1'000 \text{ K}\cdot\text{s}^{-1}$) once the synthesized nanoparticles leave the flame [27]. This quenching is assumed to be crucial for a higher degree of irreversibility of the properties of flame-spray-synthesized materials in comparison to a sol-gel method, where the cooling down is significantly slower and more controlled so that Co can easily oxidize back to a +3 state accompanied by a decrease in the oxygen vacancy concentration [8,27].

Overall, FSS is a scalable technique which can optimize the production of an oxygen-deficient BSCF with an improved electrocatalytic activity for the OER. The key for the synthesis optimization is the three investigated parameters—total metal concentration (C_{TM}) in the precursor solution, flow rate of the precursor solution (FR_{PS}) and flow rate of the dispersion gas (FR_{DG}). Changes in these parameters modify the flame condition in a way that allows BSCF production with Co, and partially Fe, in a lower oxidation state, suggesting a higher oxygen vacancy concentration, which is crucial for its high OER activity. This study shows that the three investigated FSS parameters can influence not only the specific surface area, but also have the ability to control the physico-chemical properties as the oxidation state of the elements in the synthesized materials. An open question is how a possible A-site deficiency in BSCF influences its OER activity and how this OER activity is affected when this deficiency is changing, especially in the case of the FR_{PS} and the FR_{DG} , where variations in these parameters resulted in changes in the amount of Ba- and Sr-based carbonate and nitrate secondary

phases, which could lead to a different A-site deficiency in BSCF. One of the remaining challenges in the upscaling process is the ability to produce BSCF not only with partially reduced Co, and thus with a high oxygen vacancy concentration, but also with a larger SSA_{BET} and without any secondary phases. Moreover, the limitation of a low total metal concentration must be overcome to maximize the production rate without losing the desired material properties.

4. Materials and Methods

4.1. Material Synthesis

All BSCF batches were produced with the flame spray synthesis (FSS) setup described in reference [27]. Stoichiometric amounts of barium carbonate ($BaCO_3$, $\geq 99.0\%$, Sigma-Aldrich, Buchs, Switzerland), strontium nitrate ($Sr(NO_3)_2$, $\geq 98\%$, Sigma-Aldrich, Buchs, Switzerland), cobalt nitrate hexahydrate ($Co(NO_3)_2 \cdot 6H_2O$, 99.9% , Sigma-Aldrich, Buchs, Switzerland) and iron nitrate nonahydrate ($Fe(NO_3)_3 \cdot 9H_2O$, $\geq 98\%$, Sigma-Aldrich, Buchs, Switzerland) were dissolved in a solvent mixture of ultrapure water (MicroPure UV, Thermo Fisher Scientific, Reinach, Switzerland) and acetic acid ($AcOH$, $\geq 99.0\%$, Carl Roth, Arlesheim, Switzerland) with a 75:25 volume ratio to prepare the $Ba_{0.5}Sr_{0.5}Co_{0.8}Fe_{0.2}O_{3-\delta}$ (BSCF) precursor solution. The total metal concentration (C_{TM}) in the final precursor solution was a parameter investigated during this work, studying 0.1, 0.2 and 0.3 M. The final precursor solution was then injected continuously—the flow is free of pulsation—into the spraying nozzle with the help of a flow-controlled three-piston pump (C-610, Büchi, Flawil, Switzerland). The flow rate of the precursor solution (FR_{PS}) into the flame was 10, 30 and 50 $mL \cdot min^{-1}$ for different syntheses and was also a part of the synthesis parameter investigation. The flame was formed with a combustion gas mixture of acetylene (99.6%, Carbagas, Liebefeld, Switzerland) and oxygen (99.5%, Carbagas, Liebefeld, Switzerland) with an individual flow rate of 13 and 17 $L \cdot min^{-1}$. Additionally, oxygen (99.5%, Carbagas, Liebefeld, Switzerland) was also used as dispersion gas to form the precursor solution droplets. The flow rate of the dispersion gas (FR_{DG}) was 25, 35 and 45 $L \cdot min^{-1}$ for different syntheses and was the third investigated synthesis parameter. All gas rates were set with a mass flow controller (Bronkhorst, Aesch, Switzerland). Finally, representative powder samples of around 1 g were collected with two vacuum pumps (VACFOX VC 50, Rietschle Thomas, Schopfheim, Germany) on four ashless filter papers (Whatman®, GE Healthcare, Amersham, United Kingdom).

4.2. Material Characterization

Images for the determination of the particle size and structure of the synthesized particles were acquired with transmission electron microscopy (TEM, JEM-ARM200F NEOARM operated at 200 kV, JEOL, Tokyo, Japan).

The crystalline phases of the synthesized BSCF batches were characterized using powder X-ray diffraction (XRD, SmartLab, Rigaku, Tokyo, Japan). The system was equipped with a rotating copper anode—producing the $Cu K\alpha$ radiation—and a $Cu K\beta$ filter while the X-ray beam source was operated at 40 kV and 160 mA. The powder samples were placed for each measurement on a Si-zero-background holder.

The specific surface area (SSA) of the synthesized BSCF batches were determined by applying the Brunauer–Emmett–Teller (BET) equation on N_2 adsorption isotherms (Autosorb-1, Quantachrome Instruments, Boynton Beach, FL, USA). The SSA_{BET} was normalized by the mass of the samples before the outgassing step. The samples were outgassed for 3 h at 85 °C before each measurement. The measurements were repeated three times for each BSCF batch.

The X-ray absorption spectroscopy (XAS) measurements at the Co K-edge (7709 eV) and Fe K-edge (7112 eV) were performed at the SuperXAS beamline of the Swiss Light Source (PSI, Villigen, Switzerland) using the QEXAFS setup [51]. A 2.9 T superbend magnet source provided the beamline with a polychromatic photon beam. This beam was then collimated using a Si-coated mirror followed by a channel-cut Si(111) crystal monochromator. Finally, the beam was focused to a spot size of

1 by 0.2 mm using a Rh-coated toroidal mirror. All spectra were collected in transmission mode—a linear geometry—by using three 15-cm-long ionization chambers filled with 1 bar of N₂ as detectors. Each sample was always placed between the first and second chamber with simultaneous acquisition of the Co metal reference foil between the second and third chamber. The XAS samples were pellets made from the as-synthesized BSCF batches. The same procedure was repeated for measuring standards out of cobalt(II) oxide (CoO, ≥99.99%, Sigma-Aldrich, Buchs, Switzerland), cobalt(II,III) oxide (Co₃O₄, ≥99.99%, Sigma-Aldrich, Buchs, Switzerland), iron(II) oxide (FeO, 99.7%, Sigma-Aldrich, Buchs, Switzerland) and iron(III) oxide (Fe₂O₃, ≥99.995%, Sigma-Aldrich, Buchs, Switzerland) to assign the Co and Fe oxidation state of the measured BSCF batches. Additionally, a 0.005-mm-thin Co metal foil (99.9%, GoodFellow, Huntingdon, United Kingdom) was used as reference to calibrate the energy for all measurements by setting the first maximum of the first derivative of this Co K-edge spectrum to 7709 eV. Both K-edges (Co and Fe) were measured within one scan for all samples. This QEXAFS setup at the beamline allowed for the collection of around 600 spectra, which were averaged together, in a data acquisition time of 5 min per sample. The data processing was performed with an in-house developed software called ProXAS [52].

4.3. Electrochemical Characterisation

The electrocatalytic activity for the oxygen evolution reaction (OER) of the synthesized BSCF batches was tested in a three-electrode setup using a rotating disc electrode (RDE) [53]. This setup included a multichannel potentiostat (VMP-300, BioLogic Science Instruments, Seyssinet-Pariset, France) with impedance spectroscopy (IS) capability, a modulated speed rotator (MSR, Pine Research Instrumentation, Durham, NC, USA) and a homemade cell out of a halved Nalgene fluorinated ethylene propylene (FEP) bottle (500 mL, Nalge Nunc International, Rochester, NY, USA) covered with a Teflon cap. The cell was half-filled with synthetic air (syn air, PanGas AG, Dagmersellen, Switzerland) saturated daily, freshly prepared 0.1 M potassium hydroxide solution (KOH, 99.99%, Sigma Aldrich, Buchs, Switzerland and ultrapure water (18.2 MΩ·cm (Type I⁺/I), PURELAB Chorus 1, Elga Veolia, High Wycombe, United Kingdom)). The same electrolyte was used as an internal solution for the mercury/mercury oxide (Hg/HgO, RE-61AP, ALS, Tokyo, Japan) reference electrode. All specified potentials in this study are given with respect to the reversible hydrogen electrode (RHE) scale indicated with the unit V_{RHE}. The potential difference of +0.931 V between these two scales was determined with the calibration of the used reference electrode against a polycrystalline platinum disc insert (Pt_{PC}, 5.0 mm OD (0.196 cm²), Pine Research Instrumentation, Durham, NC, USA) in the hydrogen-saturated electrolyte (for more details, refer to Figure S5 in the Supplementary Materials). All electrochemical measurements were performed at room temperature, with a freshly flame-annealed gold mesh (Gold WOVEN Mesh/Gauze, Advent Research Materials Ltd., Oxford, United Kingdom) as counter electrode and an RDE speed rate of 900 rpm.

The working electrode was prepared by drop casting 10 μL (2 × 5 μL) of a electrocatalyst containing suspension (2.0 g·L⁻¹) on a freshly polished (0.3 μm and 0.05 μm MicroPolish alumina solution used on different MicroCloths, Buehler, Lake Bluff, IL, USA) glassy carbon disc insert (GC, SIGRADUR G, 5.0 mm OD (0.2 cm²), HTW GmbH, Thierhaupten, Germany). The electrodes were dried in air with yielding an electrocatalyst loading of 0.1 mg_{oxide}·cm⁻². The suspension was produced by ultrasonically (30 min, Ultrasonic Cleaner, VWR, Radnor, PA, USA) dispersing 5 mg of the synthesized BSCF batch in a solution mixture of 2 mL 2-Propanol (IPA, 99.9% (HPLC Plus), Sigma Aldrich, Buchs, Switzerland), 0.5 mL ultrapure water (18.2 MΩ·cm (Type I⁺/I), PURELAB Chorus 1, Elga Veolia, High Wycombe, United Kingdom) and 10 μL of Na⁺-exchanged Nafion (NaOH, 99.99% and Nafion[®] perfluorinated resin solution, 5 wt % in lower aliphatic alcohols and water, contains 15–20% water, Sigma Aldrich, Buchs, Switzerland) [54].

The electrochemical protocol for determining the OER activity for the different synthesized BSCF batches included cyclic voltammetry (CV) between 1.0 and 1.7 V_{RHE} (25 times) at a scan rate of 10 mV·s⁻¹ to reach a steady-state of the increasing electrochemical surface area of the electrocatalysts

followed by chronoamperometric (CA) measurements. The steady-state current at 15 potential steps between 1.3 and 1.7 V_{RHE} was measured while holding each potential for 30 s. This steady-state current in the linear range was then plotted in a Tafel figure to determine the OER activity for the different synthesized BSCF batches. Three IS measurements were performed during this protocol, one at 1.2 V_{RHE} before the CV and two at 1.2 and 1.4 V_{RHE} after the CA measurements to determine the ionic resistance of the setup. Therefore, all applied potentials were corrected by the ohmic drop indicated in this study as $E_{\text{IR-free}}$. The current itself was normalized by the total mass ($g_{\text{oxide}} = 20 \mu\text{g}$) of the samples used during the experiment and is indicated as J in this article. Each measurement was repeated three times using two different freshly prepared electrocatalyst containing suspensions on two different days.

5. Conclusions

A systematic study was carried out to reveal the influence of the total metal concentration (C_{TM}) in the precursor solution, the flow rate of the precursor solution (FR_{PS}) and the flow rate of the dispersion gas (FR_{DG}) as flame spray synthesis (FSS) parameters on the oxygen evolution reaction (OER) activity of $\text{Ba}_{0.5}\text{Sr}_{0.5}\text{Co}_{0.8}\text{Fe}_{0.2}\text{O}_{3-\delta}$ (BSCF). The parameters were varied for each synthesis—seven in total—having three BSCF batches for each parameter investigation with one in common. The successful formation of BSCF was verified with X-ray diffraction (XRD) for each set of parameters. This study reveals that—in comparison to C_{TM} —the FR_{PS} and FR_{DG} have a significant influence on the formation of secondary phases—mostly Ba- and Sr-based carbonates and nitrates—as well as on the specific surface area (SSA_{BET}). A higher FR_{PS} and a lower FR_{DG} produces larger precursor solution droplets which enhances the probability of an incomplete decomposition of metal ion precipitations, and thus the formation of secondary phases. Moreover, a higher FR_{PS} and a lower FR_{DG} increases the high-temperature particle residence time (HTPRT) which leads to the formation of larger particles (lower SSA_{BET}). Furthermore, the study reveals that all three parameters have a direct influence on the OER activity of BSCF as well as on the Co—and to a smaller extent Fe—oxidation state in BSCF. A lower C_{TM} , a higher FR_{PS} and a lower FR_{DG} produces BSCF with a higher OER activity, with Co and Fe in a lower oxidation state. The similar trend of the Co and Fe oxidation state leads to the suggestion that the synthesis parameters can also control the oxygen vacancy concentration in BSCF. These trends confirm the hypothesis that the OER activity of BSCF is directly controlled over the initial oxidation state of Co and Fe together with the oxygen vacancy concentration. A more oxygen deficient BSCF can interact more strongly with the electrolyte to form a self-assembled and superficial oxy (hydroxide) layer (the active surface of this electrocatalyst) through the lattice OER (LOER)/OER process. The origin of the controllability of the Co and Fe oxidation state, and with that on the oxygen vacancy concentration, through the synthesis parameters lies again in the HTPRT and in the oxygen partial pressure. A longer HTPRT and a lower oxygen partial pressure, achieved with a lower C_{TM} , a higher FR_{PS} and a lower FR_{DG} , lead to the production of a more oxygen-deficient BSCF with Co, and partially Fe, in a lower oxidation state. Therefore, all three parameters directly influence the flame condition and thus the properties of the synthesized BSCF. The conclusions about the effect of these three synthesis parameters on the properties of BSCF as an OER active material can help a successful scale-up by maximizing the production rate without losing its electrocatalytic activity.

Supplementary Materials: The following are available online at <http://www.mdpi.com/2073-4344/10/9/984/s1>, Figure S1: Transmission electron microscopy (TEM) images of the common BSCF batch, Figure S2: Comparison of the X-ray diffraction (XRD) pattern of the common BSCF batch with BSCF and possible secondary phase references, Figure S3: All aligned Co K-edge X-ray absorption near edge spectroscopy (XANES) spectra of the Co metal reference foil measured simultaneously with the samples and standards at the Co K-edge, Figure S4: Comparison of Fe K-edge XANES spectra of the as-synthesized $\text{Ba}_{0.5}\text{Sr}_{0.5}\text{Co}_{0.8}\text{Fe}_{0.2}\text{O}_{3-\delta}$ (BSCF) batches, Figure S5: Recorded cyclic voltammograms (CVs) of a polycrystalline platinum disc insert (Pt_{PC}) for the reference electrode calibration in a 0.1 M potassium hydroxide (KOH) solution.

Author Contributions: Conceptualization, D.A., M.B., E.F. and T.J.S.; methodology, D.A., M.B., E.F. and T.J.S.; software, A.H.C.; validation, D.A. and M.B.; formal analysis, D.A.; investigation, D.A., M.B. and A.H.C.; resources, M.B., E.F., A.H.C., M.N., T.G. and T.J.S.; data curation, E.F., A.H.C.; writing—original draft preparation, D.A.; writing—review and editing, M.B., E.F., A.H.C., M.N., T.G. and T.J.S.; visualization, D.A.; supervision, E.F., M.N., T.G. and T.J.S.; project administration, M.N., T.G. and T.J.S.; funding acquisition, E.F., M.N., T.G. and T.J.S. All authors have read and agreed to the published version of the manuscript.

Funding: This research was funded by Innosuisse through the Swiss Competence Center for Energy Research (SCCER) Heat & Electricity Storage.

Acknowledgments: The authors gratefully acknowledge Innosuisse and the SCCER Heat & Electricity Storage. Furthermore, the authors thank the Swiss Light Source for providing beamtime at the SuperXAS beamline, the EMF at PSI for the use of their transmission electron microscope (TEM) and Elisabeth Müller for recording the TEM images.

Conflicts of Interest: The authors declare no conflict of interest.

References

1. Bp Statistical Review of World Energy 2019, 68th ed. Available online: <https://www.Bp.Com/content/dam/bp/business-sites/en/global/corporate/pdfs/energy-economics/statistical-review/bp-stats-review-2019-full-report.Pdf> (accessed on 1 February 2020).
2. Bockris, J.O. A hydrogen economy. *Science* **1972**, *176*, 1323. [[CrossRef](#)] [[PubMed](#)]
3. Abdin, Z.; Zafaranloo, A.; Rafiee, A.; Mérida, W.; Lipiński, W.; Khalilpour, K.R. Hydrogen as an energy vector. *Renew. Sustain. Energy Rev.* **2020**, *120*, 109620. [[CrossRef](#)]
4. Seh, Z.W.; Kibsgaard, J.; Dickens, C.F.; Chorkendorff, I.B.; Norskov, J.K.; Jaramillo, T.F. Combining theory and experiment in electrocatalysis: Insights into materials design. *Science* **2017**, *355*, 4998. [[CrossRef](#)] [[PubMed](#)]
5. Carmo, M.; Fritz, D.L.; Merge, J.; Stolten, D. A comprehensive review on pem water electrolysis. *Int. J. Hydrogen Energy* **2013**, *38*, 4901–4934. [[CrossRef](#)]
6. Fabbri, E.; Schmidt, T.J. Oxygen evolution reaction—the enigma in water electrolysis. *ACS Catal.* **2018**, *8*, 9765–9774. [[CrossRef](#)]
7. Fabbri, E.; Habereder, A.; Waltar, K.; Kotz, R.; Schmidt, T.J. Developments and perspectives of oxide-based catalysts for the oxygen evolution reaction. *Catal. Sci. Technol.* **2014**, *4*, 3800–3821. [[CrossRef](#)]
8. Fabbri, E.; Nachttegaal, M.; Binninger, T.; Cheng, X.; Kim, B.J.; Durst, J.; Bozza, F.; Graule, T.; Schaublin, R.; Wiles, L.; et al. Dynamic surface self-reconstruction is the key of highly active perovskite nano-electrocatalysts for water splitting. *Nat. Mater.* **2017**, *16*, 925–931. [[CrossRef](#)]
9. Kim, B.J.; Cheng, X.; Abbott, D.F.; Fabbri, E.; Bozza, F.; Graule, T.; Castelli, I.E.; Wiles, L.; Danilovic, N.; Ayers, K.E.; et al. Highly active nanoperovskite catalysts for oxygen evolution reaction: Insights into activity and stability of $\text{Ba}_{0.5}\text{Sr}_{0.5}\text{Co}_{0.8}\text{Fe}_{0.2}\text{O}_{2+\delta}$ and $\text{PrBaCo}_2\text{O}_{5+\delta}$. *Adv. Funct. Mater.* **2018**, *28*, 1804355. [[CrossRef](#)]
10. Kim, B.J.; Fabbri, E.; Abbott, D.F.; Cheng, X.; Clark, A.H.; Nachttegaal, M.; Borlaf, M.; Castelli, I.E.; Graule, T.; Schmidt, T.J. Functional role of Fe-doping in Co-based perovskite oxide catalysts for oxygen evolution reaction. *J. Am. Chem. Soc.* **2019**, *141*, 5231–5240. [[CrossRef](#)]
11. Fabbri, E.; Nachttegaal, M.; Cheng, X.; Schmidt, T.J. Superior bifunctional electrocatalytic activity of $\text{Ba}_{0.5}\text{Sr}_{0.5}\text{Co}_{0.8}\text{Fe}_{0.2}\text{O}_3$ -carbon composite electrodes: Insight into the local electronic structure. *Adv. Energy Mater.* **2015**, *5*, 1402033. [[CrossRef](#)]
12. Cheng, X.; Fabbri, E.; Kim, B.; Nachttegaal, M.; Schmidt, T.J. Effect of ball milling on the electrocatalytic activity of $\text{Ba}_{0.5}\text{Sr}_{0.5}\text{Co}_{0.8}\text{Fe}_{0.2}\text{O}_3$ towards the oxygen evolution reaction. *J. Mater. Chem. A* **2017**, *5*, 13130–13137. [[CrossRef](#)]
13. Cheng, X.; Fabbri, E.; Yamashita, Y.; Castelli, I.E.; Kim, B.; Uchida, M.; Haumont, R.; Puente-Orench, I.; Schmidt, T.J. Oxygen evolution reaction on perovskites: A multieffect descriptor study combining experimental and theoretical methods. *ACS Catal.* **2018**, *8*, 9567–9578. [[CrossRef](#)]
14. Suntivich, J.; May, K.J.; Gasteiger, H.A.; Goodenough, J.B.; Shao-Horn, Y. A perovskite oxide optimized for oxygen evolution catalysis from molecular orbital principles. *Science* **2011**, *334*, 1383–1385. [[CrossRef](#)] [[PubMed](#)]
15. Pratsinis, S.E. Aerosol-based technologies in nanoscale manufacturing: From functional materials to devices through core chemical engineering. *AIChE J.* **2010**, *56*, 3028–3035. [[CrossRef](#)]

16. Grohn, A.J.; Pratsinis, S.E.; Sanchez-Ferrer, A.; Mezzenga, R.; Wegner, K. Scale-up of nanoparticle synthesis by flame spray pyrolysis: The high-temperature particle residence time. *Ind. Eng. Chem. Res.* **2014**, *53*, 10734–10742. [[CrossRef](#)]
17. Kühner, G.; Voll, M. Manufacture of carbon black. In *Carbon Black Science and Technology*, 2nd ed.; Donnet, J.-B., Ed.; Taylor & Francis Group: New York, NY, USA, 1993; Chapter 1, pp. 1–66.
18. Grass, R.N.; Athanassiou, E.K.; Stark, W.J. Covalently functionalized cobalt nanoparticles as a platform for magnetic separations in organic synthesis. *Angew. Chem. Int. Ed.* **2007**, *46*, 4909–4912. [[CrossRef](#)]
19. Turbobeads. Available online: <http://www.Turbobeads.Com/> (accessed on 10 February 2020).
20. Shao, Z.P.; Haile, S.M. A high-performance cathode for the next generation of solid-oxide fuel cells. *Nature* **2004**, *431*, 170–173. [[CrossRef](#)]
21. Fabbri, E.; Mohamed, R.; Levecque, P.; Conrad, O.; Kotz, R.; Schmidt, T.J. Composite electrode boosts the activity of Ba_{0.5}Sr_{0.5}Co_{0.8}Fe_{0.2}O₃-Delta perovskite and carbon toward oxygen reduction in alkaline media. *ACS Catal.* **2014**, *4*, 1061–1070. [[CrossRef](#)]
22. Fabbri, E.; Mohamed, R.; Levecque, P.; Conrad, O.; Kotz, R.; Schmidt, T.J. Ba_{0.5}Sr_{0.5}Co_{0.8}Fe_{0.2}O₃-Delta perovskite activity towards the oxygen reduction reaction in alkaline media. *Chemelectrochem* **2014**, *1*, 338–342. [[CrossRef](#)]
23. Fabbri, E.; Mohamed, R.; Levecque, P.; Conrad, O.; Kotz, R.; Schmidt, T.J. Unraveling the oxygen reduction reaction mechanism and activity of d-band perovskite electrocatalysts for low temperature alkaline fuel cells. *ECS Trans.* **2014**, *64*, 1081–1093. [[CrossRef](#)]
24. Mohamed, R.; Fabbri, E.; Levecque, P.; Kotz, R.; Schmidt, T.J.; Conrad, O. Understanding the influence of carbon on the oxygen reduction and evolution activities of bscf/carbon composite electrodes in alkaline electrolyte. *ECS Trans.* **2014**, *58*, 9–18. [[CrossRef](#)]
25. Cheng, X.; Kim, B.J.; Fabbri, E.; Schmidt, T.J. Co/Fe oxyhydroxides supported on perovskite oxides as oxygen evolution reaction catalyst systems. *Acs Appl. Mater. Interfaces* **2019**, *11*, 34787–34795. [[CrossRef](#)]
26. Suntivich, J.; Gasteiger, H.A.; Yabuuchi, N.; Nakanishi, H.; Goodenough, J.B.; Shao-Horn, Y. Design principles for oxygen-reduction activity on perovskite oxide catalysts for fuel cells and metal-air batteries. *Nat. Chem.* **2011**, *3*, 546–550. [[CrossRef](#)] [[PubMed](#)]
27. Heel, A.; Holtappels, P.; Hug, P.; Graule, T. Flame spray synthesis of nanoscale La_{0.6}Sr_{0.4}Co_{0.2}Fe_{0.8}O_{3-δ} and Ba_{0.5}Sr_{0.5}Co_{0.8}Fe_{0.2}O_{3-δ} as cathode materials for intermediate temperature solid oxide fuel cells. *Fuel Cells* **2010**, *10*, 419–432. [[CrossRef](#)]
28. Chiarello, G.L.; Rossetti, I.; Forni, L. Flame-spray pyrolysis preparation of perovskites for methane catalytic combustion. *J. Catal.* **2005**, *236*, 251–261. [[CrossRef](#)]
29. Strobel, R.; Pratsinis, S.E. Effect of solvent composition on oxide morphology during flame spray pyrolysis of metal nitrates. *Phys. Chem. Chem. Phys.* **2011**, *13*, 9246–9252. [[CrossRef](#)]
30. Wegner, K.; Schimmoeller, B.; Thiebaut, B.; Fernandez, C.; Rao, T.N. Pilot plants for industrial nanoparticle production by flame spray pyrolysis. *Kona Powder Part J.* **2011**, *29*, 251–265. [[CrossRef](#)]
31. Mueller, R.; Madler, L.; Pratsinis, S.E. Nanoparticle synthesis at high production rates by flame spray pyrolysis. *Chem. Eng. Sci.* **2003**, *58*, 1969–1976. [[CrossRef](#)]
32. Mueller, R.; Jossen, R.; Pratsinis, S.E.; Watson, M.; Akhtar, M.K. Zirconia nanoparticles made in spray flames at high production rates. *J. Am. Ceram. Soc.* **2004**, *87*, 197–202. [[CrossRef](#)]
33. Grohn, A.J.; Pratsinis, S.E.; Wegner, K. Fluid-particle dynamics during combustion spray aerosol synthesis of zro2. *Chem. Eng. J.* **2012**, *191*, 491–502. [[CrossRef](#)]
34. Wegner, K.; Pratsinis, S.E. Scale-up of nanoparticle synthesis in diffusion flame reactors. *Chem. Eng. Sci.* **2003**, *58*, 4581–4589. [[CrossRef](#)]
35. Koirala, R.; Pratsinis, S.E.; Baiker, A. Synthesis of catalytic materials in flames: Opportunities and challenges. *Chem. Soc. Rev.* **2016**, *45*, 3053–3068. [[CrossRef](#)] [[PubMed](#)]
36. Messing, G.L.; Zhang, S.C.; Jayanthi, G.V. Ceramic powder synthesis by spray-pyrolysis. *J. Am. Ceram. Soc.* **1993**, *76*, 2707–2726. [[CrossRef](#)]
37. Pratsinis, S.E. Flame aerosol synthesis of ceramic powders. *Prog. Energy Combust. Sci.* **1998**, *24*, 197–219. [[CrossRef](#)]
38. Yuvaraj, S.; Lin, F.Y.; Chang, T.H.; Yeh, C.T. Thermal decomposition of metal nitrates in air and hydrogen environments. *J. Phys. Chem. B* **2003**, *107*, 1044–1047. [[CrossRef](#)]

39. Kim, B.J.; Fabbri, E.; Castelli, I.E.; Borlaf, M.; Graule, T.; Nachtegaal, M.; Schmidt, T.J. Fe-doping in double perovskite $\text{PrBaCo}_2(1-x)\text{Fe}_2\text{xO}_6$: Insights into structural and electronic effects to enhance oxygen evolution catalyst stability. *Catalysts* **2019**, *9*, 263. [CrossRef]
40. Shao, Z.P.; Yang, W.S.; Cong, Y.; Dong, H.; Tong, J.H.; Xiong, G.X. Investigation of the permeation behavior and stability of a $\text{Ba}_{0.5}\text{Sr}_{0.5}\text{Co}_{0.8}\text{Fe}_{0.2}\text{O}_3$ -Delta oxygen membrane. *J. Membr. Sci.* **2000**, *172*, 177–188. [CrossRef]
41. McIntosh, S.; Vente, J.F.; Haije, W.G.; Blank, D.H.A.; Bouwmeester, H.J.M. Oxygen stoichiometry and chemical expansion of $\text{Ba}_{0.5}\text{Sr}_{0.5}\text{Co}_{0.8}\text{Fe}_{0.2}\text{O}_3$ -delta measured by in situ neutron diffraction. *Chem. Mater.* **2006**, *18*, 2187–2193. [CrossRef]
42. McIntosh, S.; Vente, J.F.; Haije, W.G.; Blank, D.H.A.; Bouwmeester, H.J.M. Structure and oxygen stoichiometry of $\text{SrCo}_{0.8}\text{Fe}_{0.2}\text{O}_3$ -Delta and $\text{Ba}_{0.5}\text{Sr}_{0.5}\text{Co}_{0.8}\text{Fe}_{0.2}\text{O}_3$ -Delta. *Solid State Ion.* **2006**, *177*, 1737–1742. [CrossRef]
43. Svarcova, S.; Wiik, K.; Tolchard, J.; Bouwmeester, H.J.M.; Grande, T. Structural instability of cubic perovskite $\text{Ba}_x\text{Sr}_{1-x}\text{Co}_1\text{-yFe}_y\text{O}_3$ -Delta. *Solid State Ion.* **2008**, *178*, 1787–1791. [CrossRef]
44. Kotomin, E.A.; Mastrokov, Y.A.; Kuklja, M.M.; Merkle, R.; Roytburd, A.; Maier, J. First principles calculations of oxygen vacancy formation and migration in mixed conducting $\text{Ba}_{0.5}\text{Sr}_{0.5}\text{Co}_{1-y}\text{Fe}_y\text{O}_3$ -Delta perovskites. *Solid State Ion.* **2011**, *188*, 1–5. [CrossRef]
45. Yang, Z.; Harvey, A.S.; Infortuna, A.; Schoonman, J.; Gauckler, L.J. Electrical conductivity and defect chemistry of $\text{Ba}(x)\text{Sr}(1-x)\text{Co}_y\text{Fe}(1-y)\text{O}(3\text{-Delta})$ perovskites. *J. Solid State Electr.* **2011**, *15*, 277–284. [CrossRef]
46. Harvey, A.S.; Litterst, F.J.; Yang, Z.; Rupp, J.L.M.; Infortuna, A.; Gauckler, L.J. Oxidation states of Co and Fe in $\text{Ba}_{1-x}\text{Sr}_x\text{Co}_{1-y}\text{Fe}_y\text{O}_3$ -Delta ($x, y=0.2\text{--}0.8$) and oxygen desorption in the temperature range 300–1273 K. *Phys. Chem. Chem. Phys.* **2009**, *11*, 3090–3098. [CrossRef] [PubMed]
47. Grenier, J.C.; Darriet, J.; Pouchard, M.; Hagenmuller, P. Presentation of new family of perovskite type phases with vacancy ordering for formula $\text{A}_3\text{M}_3\text{O}_8$ (AMO_{2.67}). *Mater. Res. Bull.* **1976**, *11*, 1219–1226. [CrossRef]
48. Becerro, A.I.; McCammon, C.; Langenhorst, F.; Seifert, F.; Angel, R. Oxygen vacancy ordering in $\text{A}_{1-x}\text{B}_x\text{Fe}_{1-x}\text{O}_{3-\delta}$ perovskites: From isolated defects to infinite sheets. *Phase. Transit.* **1999**, *69*, 133–146. [CrossRef]
49. Scott, J.F.; Dawber, M. Oxygen-vacancy ordering as a fatigue mechanism in perovskite ferroelectrics. *Appl. Phys. Lett.* **2000**, *76*, 3801–3803. [CrossRef]
50. Eichel, R.A. Structural and dynamic properties of oxygen vacancies in perovskite oxides-analysis of defect chemistry by modern multi-frequency and pulsed EPR techniques. *Phys. Chem. Chem. Phys.* **2011**, *13*, 368–384. [CrossRef]
51. Muller, O.; Nachtegaal, M.; Just, J.; Lutzenkirchen-Hecht, D.; Frahm, R. Quick-exafs setup at the superxas beamline for in situ X-ray absorption spectroscopy with 10 ms time resolution. *J. Synchrotron Radiat.* **2016**, *23*, 260–266. [CrossRef]
52. Clark, A.H.; Imbao, J.; Frahm, R.; Nachtegaal, M. Proqexafs: A highly optimized parallelized rapid processing software for qexafs data. *J. Synchrotron Radiat.* **2020**, *27*, 551–557. [CrossRef]
53. Schmidt, T.J.; Gasteiger, H.A.; Stab, G.D.; Urban, P.M.; Kolb, D.M.; Behm, R.J. Characterization of high-surface area electrocatalysts using a rotating disk electrode configuration. *J. Electrochem. Soc.* **1998**, *145*, 2354–2358. [CrossRef]
54. Suntivich, J.; Gasteiger, H.A.; Yabuuchi, N.; Shao-Horn, Y. Electrocatalytic measurement methodology of oxide catalysts using a thin-film rotating disk electrode. *J. Electrochem. Soc.* **2010**, *157*, B1263–B1268. [CrossRef]

